

ANISOTROPIC TRAVELTIME TOMOGRAPHY

R. J. MICHELENA,² F. MUIR² and J. M. HARRIS²

ABSTRACT

MICHELENA, R.J., MUIR, F. and HARRIS, J.M. 1993. Anisotropic travelttime tomography. *Geophysical Prospecting* **41**, 381–412.

Velocity estimation technique using seismic data is often based on time/distance equations which are independent of direction, and even though we now know that many rocks are quite anisotropic, useful results have been obtained over the years from these isotropic estimates. Nevertheless, if velocities are significantly direction-dependent, then the isotropic assumption may lead to serious structural interpretation errors. Additionally, information on angle-dependence may lead to a better understanding of the lithology of the rocks under measurement. VSP and cross-well data may each lack the necessary aperture to estimate more than two velocity parameters for each wave type, and if the data straddle a symmetry axis, then these may be usefully chosen to be the direct velocities (from time-and-distance measurements along the axis) and NMO velocities (from differential time-offset measurements). These sets of two parameters define ellipses, and provide intermediate models for the variation of velocity with angle which can later be assembled and translated into estimates of the elastic moduli of the rocks under scrutiny.

If the aperture of the measurements is large enough e.g. we have access to both VSP and cross-well data, we divide the procedure into two independent steps, first fitting best ellipses around one symmetry axis and then fitting another set around the orthogonal axis. These sets of four elliptical parameters are then combined into a new, double elliptical approximation. This approximation keeps the useful properties of elliptical anisotropy, in particular the simple relation between group and phase velocities which simplifies the route from the traveltimes measurements to the elastic constants of the medium.

The inversion proposed in this paper is a simple extension of well-known isotropic schemes and it is conceptually identical for all wave types. Examples are shown to illustrate the application of the technique to cross-well synthetic and field P-wave data. The examples demonstrate three important points: (a) When velocity anisotropy is estimated by iterative

¹ Paper presented in two parts at the 53rd EAEG meeting, Florence, May 1991. Received January 1992, revision accepted September 1992.

² Department of Geophysics, Stanford University, Stanford, CA 94305, U.S.A.

techniques such as conjugate gradients, early termination of the iterations may produce artificial anisotropy. (b) Different components of the velocity are subject to different type of artifacts because of differences in ray coverage. (c) Even though most rocks do not have elliptical dispersion relations, our elliptical schemes represent a useful intermediate step in the full characterization of the elastic properties.

INTRODUCTION

Depending on the degree of anisotropy and fine layering of the medium, tomograms obtained from cross-well traveltimes data under an isotropic assumption may be significantly in error. These errors are analogous to the mispositions in surface seismic when, in an anisotropic environment, stacking velocities are used to convert times into depths. Eliminating these errors provides the main reason for allowing the model to be anisotropic in tomographic traveltimes inversion. Another is that we are solving more than an imaging problem, since it is well known that anisotropy is a useful tool for studying lithology and the degree of stratification in sedimentary rocks. Taking velocity anisotropy into account in tomographic traveltimes inversion adds useful information about reservoir and non-reservoir rocks.

From surface seismic measurements, whether reflection or refraction, it is possible to obtain the horizontal component of the slowness. For estimating anisotropy additional subsurface information (layer thicknesses or vertical slownesses) is required (Levin 1978). For this reason, in recent studies where anisotropy has been quantified, either a different geometry such as VSP has been used (Byun and Corrigan 1990; White, Martineau-Nicoletis and Monash 1983) or the surface seismic information has been combined with well logs (Banik 1984). Based on the observation that velocity anisotropy does not affect P-wave moveout considerably, Winterstein (1986) estimated the required layer thicknesses using velocities obtained from P-wave velocity analysis. Then, from SH-wave velocity analysis, he was able to estimate velocity anisotropy. Dellinger (1989) concluded that because of the ill-conditioning of the problem, it is not possible to estimate with high accuracy a 2D vector velocity field from VSP-like geometries.

Fewer attempts have been made to estimate velocity anisotropy from cross-well measurements. Stewart (1988) proposed a modification to ART methods to estimate velocity anisotropy. By using the weak anisotropy expression for the phase velocities given by Thomsen (1986) to fit the traveltimes, Stewart appeared to assume the equality of group and phase velocities, which is, in general, not true. Winterstein and Paulsson (1990) estimated a vertical velocity gradient from VSP and cross-well data assuming a transversely isotropic model. More recently, Chapman and Pratt (1992) and Pratt and Chapman (1992) estimated velocity anisotropy in a general 2D medium assuming weak anisotropy in order to justify isotropic ray tracing.

The main difference between tomographic velocity estimation from surface measurements and cross-well or VSP traveltimes is that the former requires *a priori* knowledge of reflector positions whereas the others do not. The only positions needed to estimate velocities from direct path cross-well traveltimes are the source and receiver locations. By eliminating reflector mapping from the problem, the esti-

mation of other effects such as velocity anisotropy may be simpler in the cross-well environment.

Elliptical anisotropy is the simplest model of anisotropy, since it introduces only one more degree of freedom, and wave and ray relationships are quite similar to the isotropic case. However, elliptical anisotropy may be an appropriate approximation in only a few cases, such as when the departure from isotropy is small or when the observations are limited to a narrow range of angles about a symmetry plane or axis. To solve such a dilemma between the convenient properties of elliptical anisotropy and its restricted applicability, Muir (1990) proposed an approximation that fits a wider range of transversely isotropic media while maintaining the useful properties of elliptical anisotropy. Dellinger, Muir and Karrenbach (1993) studied in detail the properties of this approximation.

Muir's approximation is based on four elliptical parameters: two (S_x and $S_{z\text{NMO}}$) for the near horizontal propagation (cross-well) and two (S_z and $S_{x\text{NMO}}$) for the near vertical propagation (VSP). Each pair of parameters can be estimated by fitting an elliptical relation to the traveltimes measured for each geometry. For this reason, Muir's approximation has been called double elliptical approximation.

We show how to estimate tomographically the elliptical parameters needed in the double elliptical approximation, in particular those corresponding to cross-well geometries. The slowness components S_x and $S_{x\text{NMO}}$ are estimated *simultaneously*, without using any additional information. The technique presented here generalizes the idea of tomographic inversion in isotropic media (McMechan 1983) where the model is discretized into orthogonal regions and the Jacobian is related to the intersection of the rays with all those regions.

There are two important differences between our method and that discussed by Chapman and Pratt (1992) and Pratt and Chapman (1992). Whereas they estimate five parameters from the pseudo-P data alone, but with fewer symmetry assumptions, we make no attempt to estimate more than two parameters (direct and moveout velocities) for each wave type from each of the two data sets, cross-well and VSP. Also, we make no assumption on the weakness of the anisotropy whereas Chapman and Pratt do. Their assumption leads them to use an isotropic ray-tracing scheme, our scheme allows us to use the well-known closed-form relationship between ray and wave velocities in elliptical media.

We study the effects of the limited view of the measurements (from cross-well geometries) in the estimation of both slowness components, concluding that our technique is stable when used to invert 1D (layered) models if the range of ray angles is 'wide enough'. In 2D models, the estimation of lateral variations in the vertical component of the slowness is particularly difficult from cross-well geometries alone. Consequently, 2D spatial variations in velocity anisotropy cannot be estimated at the same scale of variations in velocity. We also show that when iterative techniques such as conjugate gradients are used to invert for the anisotropic parameters, early termination of the iterations may produce artificial anisotropy. This problem worsens in 2D.

We first explain what the double elliptical approximation is and which parameters need to be estimated in order to use it. We then explain how those parameters

can be actually estimated in particular for a cross-well geometry. The theory presented is illustrated with synthetic examples and applications to field data from a cross-well geometry.

DOUBLE ELLIPTICAL APPROXIMATION

We summarize the results contained in Dellinger *et al.* (1993) and Muir (1991).

Phase velocity around the axis of symmetry and perpendicular to it

The phase velocity expression for P- and SV-waves in a transversely isotropic media is (Auld 1990)

$$2W(\theta) = (W_{33} + W_{44}) \cos^2 \theta + (W_{11} + W_{44}) \sin^2 \theta \\ \pm \sqrt{\frac{[(W_{33} - W_{44}) \cos^2 \theta - (W_{11} - W_{44}) \sin^2 \theta]^2}{+ 4(W_{13} + W_{44})^2 \sin^2 \theta \cos^2 \theta}}$$

where $W(\theta)$ is the phase velocity squared and θ is the phase angle from the vertical W_{ij} is the (ij)th elastic modulus divided by density, with units of velocity squared. The plus sign in front of the square root corresponds to P-waves and the minus to SV-waves. After expanding the previous expression around $\theta = 0$ and neglecting terms in $\sin^4 \theta$, we obtain

$$2W(\theta) = (W_{33} + W_{44}) \cos^2 \theta + (W_{11} + W_{44}) \sin^2 \theta \\ \pm \left((W_{33} - W_{44}) \cos^2 \theta - (W_{11} - W_{44}) \sin^2 \theta + \frac{2(W_{13} + W_{44})^2}{W_{33} - W_{44}} \sin^2 \theta \right). \quad (1)$$

Choosing the plus sign we get the P-wave phase velocity around the vertical axis, given by

$$W(\theta) = W_{P,z} c^2 + W_{P,xNMO} s^2, \quad (2)$$

where $c = \cos \theta$, $s = \sin \theta$,

$$W_{P,z} = W_{33}, \quad (3)$$

and

$$W_{P,xNMO} = W_{44} + \frac{(W_{13} + W_{44})^2}{W_{33} - W_{44}}. \quad (4)$$

$W_{P,z}$ is the vertical phase velocity squared and $W_{P,xNMO}$ is the horizontal moveout velocity squared.

Similarly, we can obtain P-wave phase velocity around the horizontal axis by interchanging W_{11} and W_{33} and c^2 and s^2 wherever they occur in (2), i.e.

$$W(\theta) = W_{P,x} s^2 + W_{P,zNMO} c^2, \quad (5)$$

where

$$W_{P,x} = W_{11}, \quad (6)$$

and

$$W_{P,zNMO} = W_{44} + \frac{(W_{13} + W_{44})^2}{W_{11} - W_{44}}. \quad (7)$$

Choosing the minus sign in (1), we get the SV-wave phase velocities around the vertical axis, given by

$$W(\theta) = W_{SV,z} c^2 + W_{SV,xNMO} s^2, \quad (8)$$

where

$$W_{SV,z} = W_{44}, \quad (9)$$

and

$$W_{SV,xNMO} = W_{11} - \frac{(W_{13} + W_{44})^2}{W_{33} - W_{44}}. \quad (10)$$

The expression that describes SV-wave phase velocity around the horizontal axis is

$$W(\theta) = W_{SV,x} s^2 + W_{SV,zNMO} c^2, \quad (11)$$

where

$$W_{SV,x} = W_{44}, \quad (12)$$

and

$$W_{SV,zNMO} = W_{33} - \frac{(W_{13} + W_{44})^2}{W_{11} - W_{44}}. \quad (13)$$

Hereafter we refer to $W_{P,x}$, $W_{P,z}$, $W_{P,xNMO}$, $W_{P,zNMO}$, $W_{SV,x}$, $W_{SV,z}$, $W_{SV,xNMO}$ and $W_{SV,zNMO}$ as W_* , direct or NMO phase velocity squared for P- and SV-waves.

Ray velocity around the axis of symmetry and perpendicular to it

We have just seen that close to the horizontal and vertical axes the phase velocity for P- and SV-waves is elliptical. It has been shown (Levin 1978; Byun 1982) that when the phase velocity has elliptical shape the corresponding impulse response is also elliptical. Therefore, the group slowness expression that corresponds to (2), (5), (8) and (11) has the general form

$$S^2(\phi) = S_z^2 \cos^2 \phi + S_x^2 \sin^2 \phi, \quad (14)$$

where ϕ is the ray angle measured from the vertical and S_* (ray slowness) is given by

$$S_*^2 = \frac{1}{W_*}. \quad (15)$$

The traveltimes equation for a ray that travels a distance $l = \sqrt{\Delta x^2 + \Delta z^2}$ between two points is obtained by multiplying $l^2 S^2(\phi)$, resulting in

$$t^2 = \Delta x^2 S_x^2 + \Delta z^2 S_z^2, \quad (16)$$

which has the same form as the isotropic moveout equation. Velocities estimated from the moveout around one axis using this equation are called NMO velocities and velocities estimated from arrival times along the same axis are called direct velocities. Hence the different names chosen for the phase velocities around the axes (W_*).

Double elliptical approximation

The parameters S_* (ray slownesses) can be estimated by fitting traveltimes data with traveltimes equations such as (16) around the horizontal and vertical axes. From S_* we can also estimate the elliptical phase velocity parameters W_* by using (15). The parameters W_* estimated in this way are useful, not only to approximate the slowness surface around the axes, but also at intermediate angles when the following expression is used:

$$W(\theta) = \frac{W_x^3 s^6 + W_x^2 (2W_z + W_{z\text{NMO}}) s^4 c^2 + (2W_x + W_{x\text{NMO}}) s^2 c^4 + W_z^3 c^6}{(W_x s^2 + W_z c^2)^2}. \quad (17)$$

This approximation is called double elliptical because it uses the elliptical parameters estimated around horizontal and vertical axes. Its derivation is shown in the Appendix. Around the axis of symmetry and perpendicular to it, the previous expression has elliptical shape, which can be verified by taking the limit $\theta \approx 0$ and $\theta \approx \pi/2$. An approximation of the same functional form can be obtained for the group velocities.

Figures 1 and 2 show how the approximation works in fitting the P slowness surface and impulse response. Note that around the horizontal the approximation is effective at angles close to 40° . Close to the vertical it is good for smaller angles. Figure 3 shows how the approximation works in fitting the SV impulse response. Notice that it cuts out triplications. However, it is much better in fitting the slowness surface (where there are no triplications) as shown in Fig. 4.

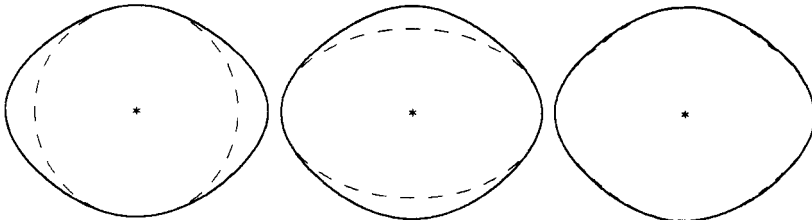


FIG. 1. Three different approximations (dashed curves) to the P impulse response. Left: vertical paraxial elliptical approximation (obtained from VSP data, for example). Centre: horizontal paraxial elliptical approximation (obtained from cross-well traveltimes). Right: Muir's double elliptical approximation. (Dellinger *et al.* 1993).

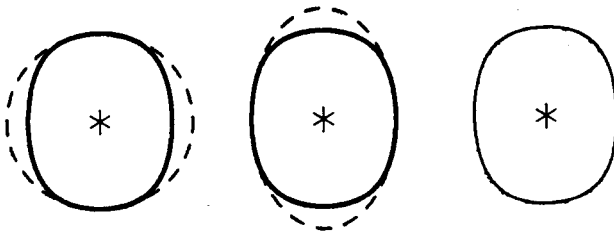


FIG. 2. Three different approximations (dashed curves) to the P slowness surface. Left: vertical paraxial elliptical approximation. Centre: horizontal paraxial elliptical approximation. Right: double elliptical approximation. (Dellinger *et al.* 1993).

From traveltimes to elastic constants

For a given density and provided P- and SV-data around the horizontal and vertical axes are available, (3), (4), (6), (7), (9), (10), (12) and (13) form an over-determined system of equations that relates four of the elastic constants of a transversely isotropic medium with W_* , the latter being estimated from traveltimes using (16) and (15). P- and SV-traveltimes around the horizontal and vertical axes can be

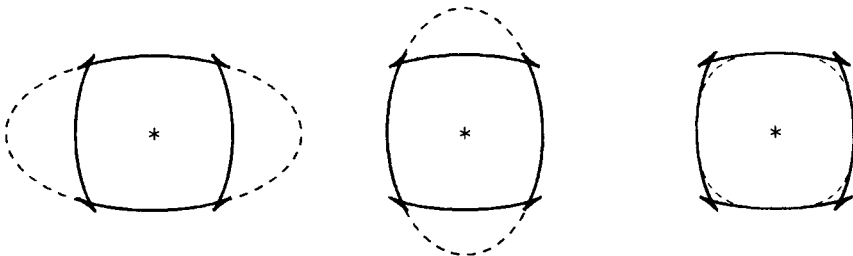


FIG. 3. Three different approximations (dashed curves) to the SV impulse response. Left: vertical paraxial elliptical approximation. Centre: horizontal paraxial elliptical approximation. Right: double elliptical approximation. (Dellinger *et al.* 1993).

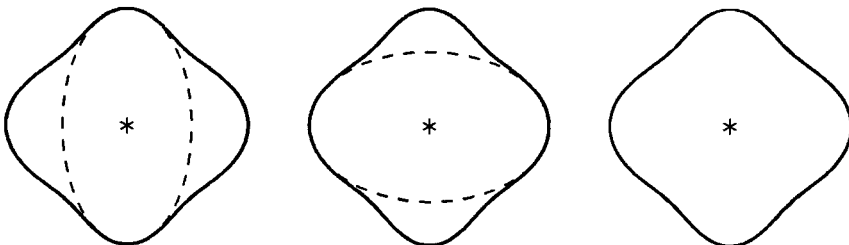


FIG. 4. Three different approximations (dashed curves) to the SV slowness surface. Left: vertical paraxial elliptical approximation. Centre: horizontal paraxial elliptical approximation. Right: double elliptical approximation. The agreement is so good for this example that the dashed curve is hard to see. (Dellinger *et al.* 1993).

measured with cross-well and VSP-like geometries, for example. Therefore, in order to use the double elliptical approximation to estimate elastic constants an inversion procedure is needed that fits traveltimes with ellipses described by the parameters S_* .

FORWARD MODELLING

We start by defining the equations needed to perform the forward modelling step in the inversion algorithm. In a homogeneous elliptical medium with a vertical symmetry axis, the traveltime between two different points separated by a distance l is the square root of (16), i.e.

$$t = \sqrt{\Delta x^2 S_x^2 + \Delta z^2 S_z^2}. \quad (18)$$

S_x and S_z are the horizontal and vertical slownesses respectively. Since the medium is homogeneous, the raypath is straight.

A heterogeneous medium can be approximated as a superposition of non-overlapping homogeneous regions. For this medium, the previous expression for the traveltime between two points can be easily generalized as follows:

$$\begin{aligned} t_i &= \sum_{j=1}^N \sqrt{\Delta x_{ij}^2 S_{x_j}^2 + \Delta z_{ij}^2 S_{z_j}^2}, \quad i = 1, \dots, M, \\ &= \sum_{j=1}^N t_{ij}, \end{aligned} \quad (19)$$

where t_{ij} is the traveltime of the i th ray in the j th cell and S_{x_j} , and S_{z_j} are the horizontal and vertical slownesses respectively in that cell. Δx_{ij} and Δz_{ij} are the horizontal and vertical distances travelled by the i th ray in the j th cell. If the slowness contrasts among adjacent cells are small, the raypaths can be approximated by straight lines. For larger contrasts, rays bend at each interface according to Snell's law. In (19), N is the total number of cells and M is the total number of traveltimes.

The slowness model can be seen as a vector \mathbf{s} whose components contain the horizontal and vertical slownesses of each cell. This vector can be defined as follows:

$$S_i = S_{x_i} \quad (30a)$$

$$S_{i+N} = S_{z_i}. \quad (30b)$$

Then, the slowness vector \mathbf{s} has the following form:

$$\mathbf{s} = (S_1, S_2, \dots, S_N, S_{N+1}, S_{N+2}, \dots, S_{2N})^T \quad (21)$$

where T means transpose. The first N components correspond to the horizontal slownesses of all the cells and the second N components correspond to the vertical slownesses. When the model is homogeneous, \mathbf{s} is 2-dimensional and in general, for a heterogeneous model described by N cells, \mathbf{s} is $2N$ -dimensional.

Using the new notation introduced in (20), the traveltime equation (19) can be written as

$$t_i = t_i(\mathbf{s}) = \sum_{j=1}^N \sqrt{\Delta x_{ij}^2 S_j^2 + \Delta z_{ij}^2 S_{j+N}^2}. \quad (22)$$

Notice that when the medium is isotropic ($S_j = S_{j+N}$), (22) reduces to the familiar equation that approximates the traveltimes computed in an isotropic model described by cells (McMechan, 1983),

$$\begin{aligned} t_i &= \sum_{j=1}^N S_j \sqrt{\Delta x_{ij}^2 + \Delta z_{ij}^2}, \\ &= \sum_{j=1}^N S_j l_{ij}, \end{aligned} \quad (23)$$

where l_{ij} is the length of the i th ray in the j th cell.

In the next section we see that when (22) is linearized, it can be used for estimating the horizontal and vertical slownesses in a heterogeneous anisotropic model given a set of traveltime measurements from a cross-well configuration. Equation (22) can also be used for surface geometries, as long as the depths of the reflectors are known *a priori*.

INVERSE MODELLING

Homogeneous model

Expression (22) will be used as a starting point to estimate the $2N$ -dimensional slowness vector \mathbf{s} given the traveltimes from a cross-well experiment. However, we can investigate some of the difficulties in estimating such a vector by first studying the case of a homogeneous medium ($N = 1$).

When the model is isotropic, we usually estimate the slowness S of the homogeneous medium that best fits the traveltimes by simply averaging all the slownesses S_i obtained from the individual rays,

$$S = \frac{1}{M} \sum_{i=1}^M S_i = \frac{1}{M} \sum_{i=1}^M \frac{t_i}{l_i}, \quad (24)$$

where l_i is the source–receiver distance and M is the total number of traveltimes.

When the model is anisotropic, the 2D vector \mathbf{s} that best fits the traveltimes can be obtained by generalizing the average (24). This generalization is, as expected, in a least-squares sense. Note that (16) is linear in S_x^2 and S_z^2 . Therefore, for a given set of traveltimes and source–receiver locations, it is possible to set up a least-squares problem to find the vector \mathbf{s} of the homogeneous medium. Defining $M_x = S_x^2$ and $M_z = S_z^2$, the least-squares problem is

$$\mathbf{M} \begin{pmatrix} M_x \\ M_z \end{pmatrix} = \mathbf{d}, \quad (25)$$

where

$$\mathbf{M} = \begin{pmatrix} \Delta x_1^2 & \Delta z_1^2 \\ \Delta x_2^2 & \Delta z_2^2 \\ \vdots & \vdots \\ \Delta x_M^2 & \Delta z_M^2 \end{pmatrix},$$

and

$$\mathbf{d} = \begin{pmatrix} t_1^2 \\ t_2^2 \\ \vdots \\ t_M^2 \end{pmatrix}.$$

Equation (25) can be solved in different ways. The most common approach is by using the normal equations, giving

$$\begin{pmatrix} M_x \\ M_z \end{pmatrix} = (\mathbf{M}^T \mathbf{M})^{-1} \mathbf{M}^T \mathbf{d}. \quad (26)$$

However, the normal equations may have undesirable features with respect to numerical stability because the condition number of $\mathbf{M}^T \mathbf{M}$ is the square of the condition number of \mathbf{M} . If \mathbf{M} is only moderately ill-conditioned, $\mathbf{M}^T \mathbf{M}$ is severely ill-conditioned. For this reason, methods that do not amplify the condition number of \mathbf{M} should be used to solve systems such as (25) (for example QR factorization, Gill, Murray and Wright 1991).

For estimating M_x and M_z *simultaneously and accurately*, \mathbf{M} has to be well conditioned. Note that this is not the case when most of the elements of the matrix satisfy either $\Delta x_i^2 \gg \Delta z_i^2$ or $\Delta z_i^2 \gg \Delta x_i^2$. These two conditions describe cases when most rays are travelling close to the horizontal or the vertical. In such cases, it is impossible to determine simultaneously both components of the vector \mathbf{s} because the limited view of the measurements translates immediately into severe ill-conditioning. This can be understood by trying to estimate M_x and M_z from the simple cross-well experiment shown in Fig. 5, where $\Delta x^2 \gg \Delta z_i^2$. In this case

$$\mathbf{M} = \begin{pmatrix} \Delta x^2 & \Delta z_1^2 \\ \Delta x^2 & \Delta z_2^2 \end{pmatrix}.$$

The eigenvalues of this matrix are

$$\lambda_{\pm} = \frac{\Delta x^2 + \Delta z_2^2 \pm \sqrt{(\Delta x^2 - \Delta z_2^2)^2 + 4\Delta x^2 \Delta z_1^2}}{2}.$$

Since $\Delta x^2 \gg \Delta z_i^2$, the eigenvalues to the first order are

$$\lambda_+ \approx \Delta x^2 + \Delta z_1^2,$$

$$\lambda_- \approx \Delta z_2^2 - \Delta z_1^2.$$

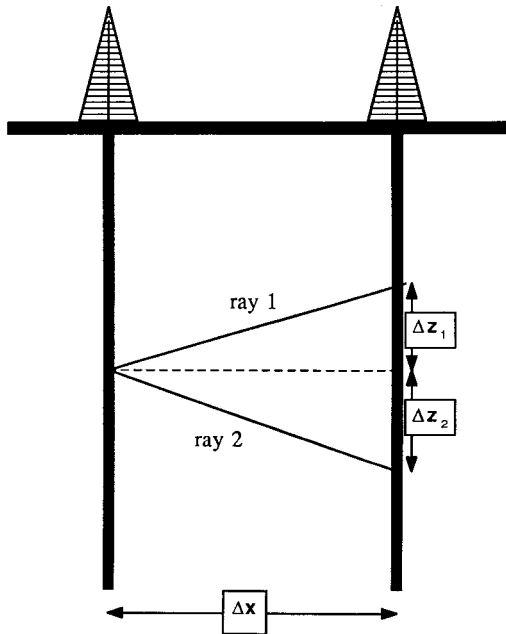


FIG. 5. Cross-well experiment with two rays.

The largest eigenvalue is related to the horizontal component of the slowness and the smallest one is related to the vertical component. In contrast, for a VSP-like geometry the largest eigenvalue is related to S_z and the smallest one is related to S_x (Dellinger 1989). Having more rays (M) without increasing the aperture does not solve the problem. In such a case, the largest eigenvalue of the matrix ($\mathbf{M}^T \mathbf{M}$) tends to $\sum_{i=1}^M \Delta x_i^2$ and the smallest one tends to zero again.

The previous inversion scheme ignores the estimation of the horizontal and vertical component of the slowness for heterogeneous models.

Heterogeneous model

Equation (22) can be used as starting point to estimate \mathbf{s} for *all* the cells at the same time. This equation is obviously non-linear in S_j and S_{j+N} . One way to solve the problem is by a sequence of linearized steps. We start by approximating (22) by a first-order Taylor series expansion centred in a given model \mathbf{s}_0 :

$$\begin{aligned}
 t_i(\mathbf{s}) &\approx t_i(\mathbf{s}_0) + \nabla t_i(\mathbf{s}_0) \cdot (\mathbf{s} - \mathbf{s}_0) \\
 &= t_i(\mathbf{s}_0) + \sum_{j=1}^{2N} \mathbf{J}_{ij}(S_j - S_{0j}),
 \end{aligned}
 \tag{27}$$

where the elements of the Jacobian \mathbf{J}_{ij} are

$$\mathbf{J}_{ij} = \frac{\partial t_{ij}(\mathbf{s}_0)}{\partial S_j} = \begin{cases} \frac{\Delta x_{ij}^2 S_{0j}}{t_{ij}}, & \text{if } 1 \leq j \leq N, \\ \frac{\Delta z_{ij}^2 S_{0j}}{t_{ij}}, & \text{if } N + 1 \leq j \leq 2N, \end{cases}$$

and t_{ij} is the traveltimes of the i th ray in the j th cell of the model \mathbf{s}_0 (equation (19)). If we assume that $t_i(\mathbf{s})$ represents one component of the vector of measured traveltimes, we can compute the perturbations $\Delta s_j = (S_j - S_{0j})$ once the traveltimes in the reference model \mathbf{s}_0 have been calculated. The perturbation $\Delta \mathbf{s} = (\mathbf{s} - \mathbf{s}_0)$ is the solution of the following system of equations

$$\mathbf{J} \Delta \mathbf{s} = \Delta \mathbf{t} \tag{28}$$

where $\Delta t_i = t_i(\mathbf{s}) - t_i(\mathbf{s}_0)$.

Note that the matrix \mathbf{J} depends *explicitly* on the slowness of the reference model \mathbf{s}_0 in contrast to the isotropic case where the matrix depends only on the lengths of the rays at each pixel. In the isotropic case if the rays are straight, the estimation of the slowness becomes a linear problem because \mathbf{J} is a constant. In the anisotropic case, however, the problem is still non-linear even if the rays are straight. Ray bending introduces another source of non-linearity.

When the model is isotropic and 2D, the largest singular values of the Jacobian correspond roughly to horizontal structures in the model and the smallest to vertical structures (Bregman, Bailey and Chapman 1989; Pratt and Chapman 1992). When the model is elliptically anisotropic, Michelena (1993) has shown that the smallest singular values of the problem correspond, in model space, to horizontal variations in the vertical component of the slowness, whereas the largest ones correspond to vertical variations in the horizontal component, which is roughly a combination of the results obtained for anisotropic homogeneous and isotropic heterogeneous models. This means that estimating S_x in layered models is an easier problem than estimating S_z in 2D models, as will be shown in the examples. Michelena (1993) also showed that in data space the largest singular values of \mathbf{J} correspond to traveltimes in the far vertical offsets.

In the examples shown later, (28) will be solved using the LSQR variant of the conjugate gradient algorithm (Nolet 1987). We show that after a few iterations with this method at each linearized step, the ill-conditioning of \mathbf{J} caused by the limited view of the measurements is better handled than by solving the normal equations.

Meaning of the results

Isotropic tomography fits the data with circles ($t^2 = (x^2 + z^2)S^2$). Anisotropic tomography, as presented, uses ellipses ($t^2 = x^2 S_x^2 + z^2 S_z^2$) instead of circles. Depending on the range of ray angles available (or the geometry used) and the wave type under consideration, the estimated slownesses S_x and S_z may or may not corre-

respond to the real slownesses of the medium. In the cross-well synthetic examples that follow, the estimated slownesses are S_x and S_z because the synthetic models used are elliptically anisotropic. In the real data examples, the estimated slownesses are S_x and $S_{z\text{NMO}}$ since the vertical slowness of the best-fitting ellipses are not necessarily the same as the true vertical slownesses S_z from sonic logs. We shall see, however, that $S_{z\text{NMO}}$ is closer and better correlated to the sonic log than S_x .

SYNTHETIC EXAMPLES

1D inversion

We now apply the previous technique to the inversion of traveltimes for a cross-well geometry. Synthetic data were generated through the 1D isotropic model shown in Fig. 6, using a geometry of 17 sources and 17 receivers equally spaced at the source and receiver well respectively. If we plot the components of the slowness vector \mathbf{s} (equation (21)) for this model, we obtain the profile shown at the right-hand side of Fig. 6. Both slowness components are identical because the model is isotropic. In this example, the slowness contrast between the background and the anomalous layer is small (1%) and therefore, the propagation of the energy can be safely modelled by straight raypaths.

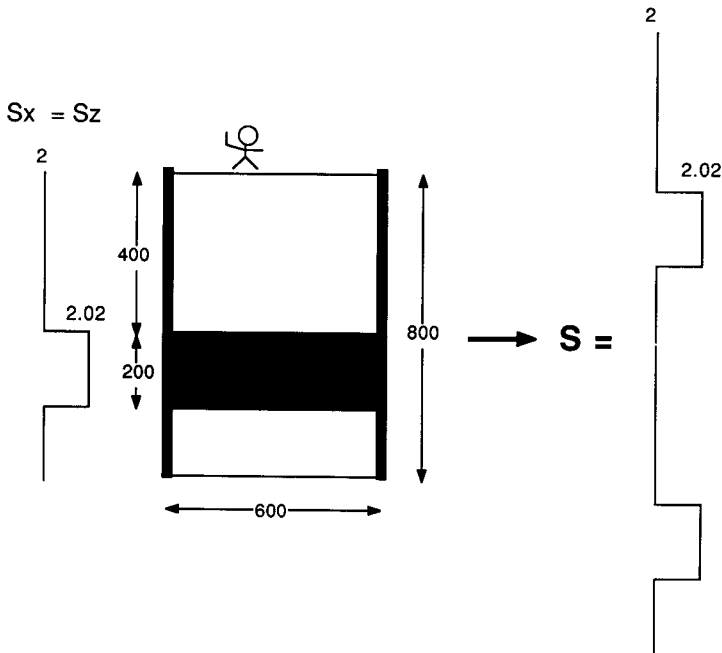


FIG. 6. Synthetic isotropic model used to test the algorithm. The slowness vector \mathbf{s} that describes this model is shown on the right.

The inversion can be constrained by allowing only vertical variations in the model if it is known *a priori* that the medium is layered. By doing this, we eliminate instabilities and non-uniqueness in the inversion associated with lateral variations, retaining only those associated with the vertical component of the slowness, which is not sampled sufficiently by the cross-well recording geometry.

The image area was divided into 100 layers of equal thickness (8 ft.). The inversion process has to estimate 200 parameters from 289 traveltimes. Figure 7 shows the slowness vector obtained after 60 conjugate gradients (CG) iterations. There is no difference between the given S (Fig. 6) and the estimated one (Fig. 7). Note also that the results can be represented as a function of depth as well as a function of the index of the slowness vector. In the next two results the depth axis will be omitted.

Figure 8 shows the convergence as a function of the CG iterations. The result shown in Fig. 7 corresponds in Fig. 8 to 60 CG iterations in the axis *number of iterations*. The two 'hills' represent the slowness at the anomalous layer. Convergence is achieved when the top and the bottom of the hills are flat. Note that the horizontal component of the slowness converges faster than the vertical component. This is because in the given model, the horizontal component of the slowness in the anomalous layer is better sampled than the vertical component: the range of ray angles (absolute values) is from 0 to 53° ($53 \approx \arctan(\frac{800}{600})$) which is a typical range for cross-well experiments.

When synthetic data is generated through the model shown at the top of Fig. 9 (where the well-to-well separation has been decreased), both components converge at the same rate. This is because the vertical component of the slowness is better

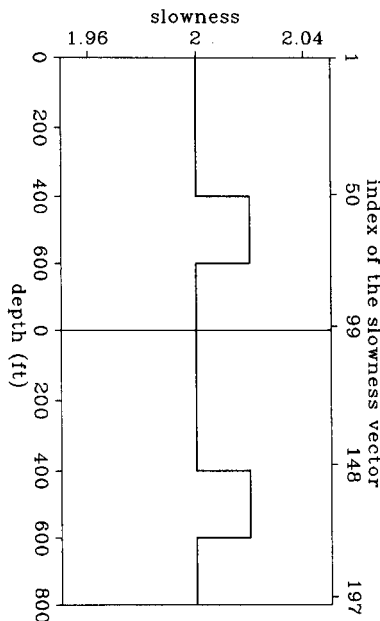


FIG. 7. Result of the inversion of the synthetic data generated by the model shown in Fig. 6.

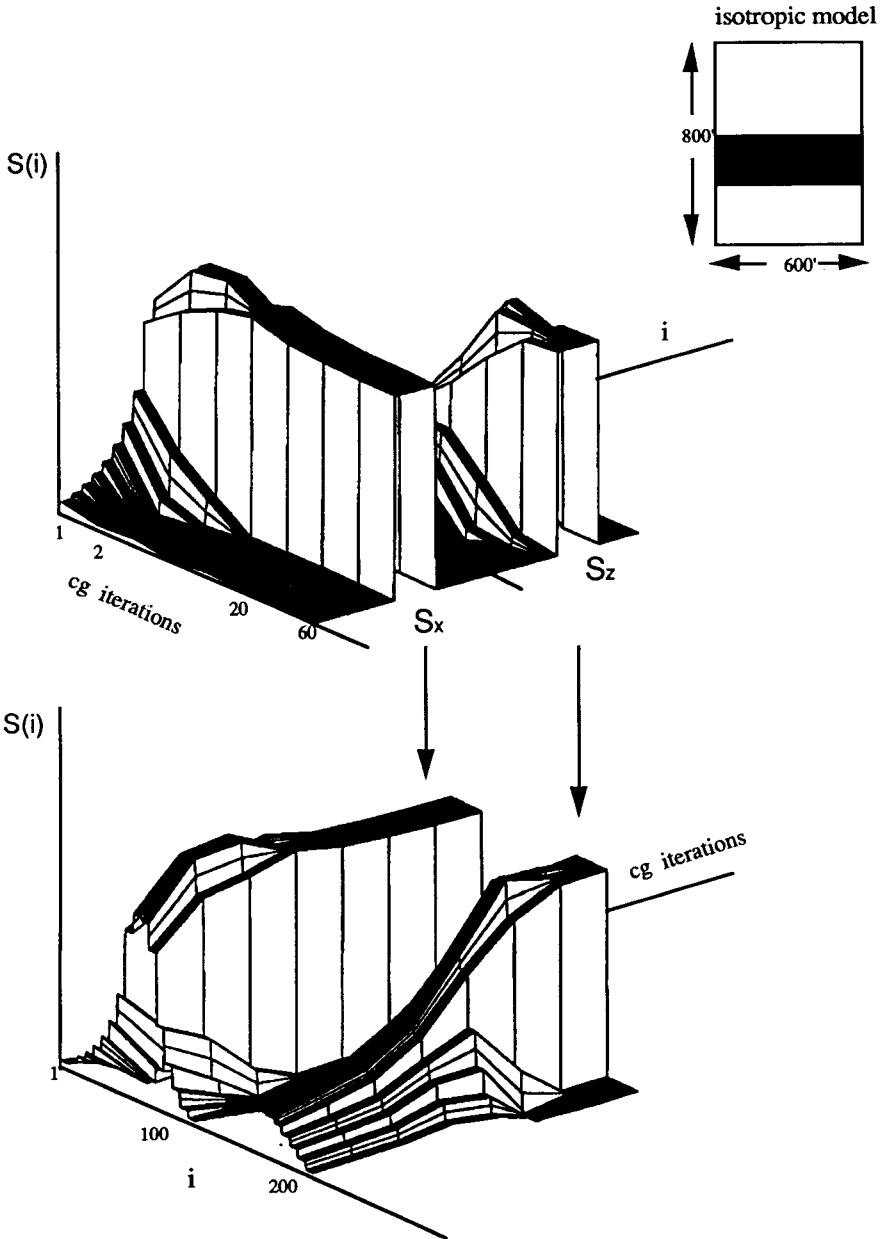


FIG. 8. Variations of the slowness vector as a function of the number of conjugate gradient iterations. The original model is shown at the top. The axes ' i ' and 'CG iterations' have been interchanged from one plot to the other.

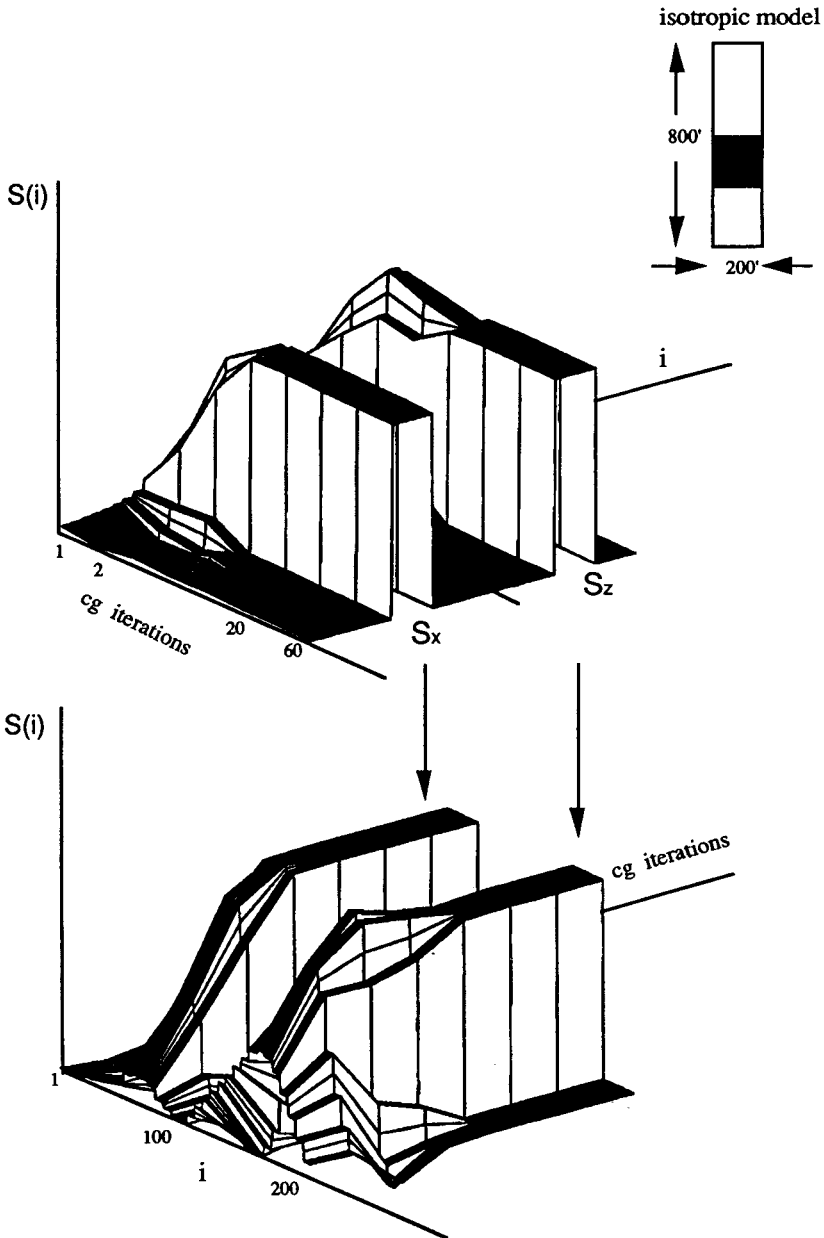


FIG. 9. Variations of the slowness vector as a function of the number of conjugate gradient iterations. The only difference between the model shown at the top and the model of Fig. 8 is in the horizontal dimension. The axes ' i ' and 'CG iterations' have been interchanged from one plot to the other.

sampled now than before: the range of ray angles varies between 0 and 76° ($76 \approx \arctan(\frac{800}{200})$).

The previous results tell us that if it is not possible to perform 'enough' CG iterations in order to reach the flat top of both hills (Figs 8 and 9), we may wrongly conclude that the medium is anisotropic because the components of the slowness vector may not converge at the same rate. Severe limited-view problems as well as low signal-to-noise ratios are some reasons that may limit the number of CG iterations that can be performed before the smallest singular values of the problem start playing any role.

2D inversion

To test the performance of the algorithm in inverting data generated in a 2D model, we computed synthetic traveltimes through the isotropic model shown in Fig. 10. The separation between contiguous sources and receivers is 10 ft and for each receiver gather, only sources located at $\pm 50^\circ$ are used. With a geometry like this, we pretend to simulate the geometry of the real data example to be analysed later. As in the 1D example, the slowness contrast between the anomaly and the background is small (5%), and therefore, straight rays can again be used.

The unknown model was discretized into 241×46 pixels (5×5 ft²) and therefore, the inversion has to estimate $241 \times 46 \times 2$ parameters from 2200 synthetic traveltimes. Figure 11 shows the results of the inversion. The slowness of the isotropic circular anomaly (1.05) is better estimated by the horizontal than by the

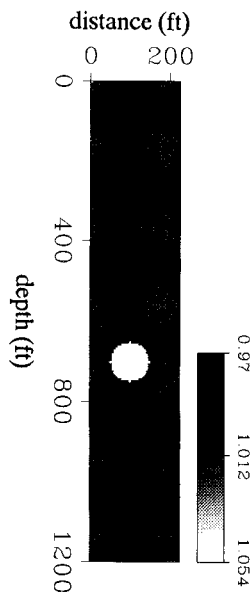


FIG. 10. Isotropic slowness model. The radius of the circular anomaly is $r = 50$ and is centred at (100, 700). The background slowness is 1.0 and the slowness of the disc is 1.05.

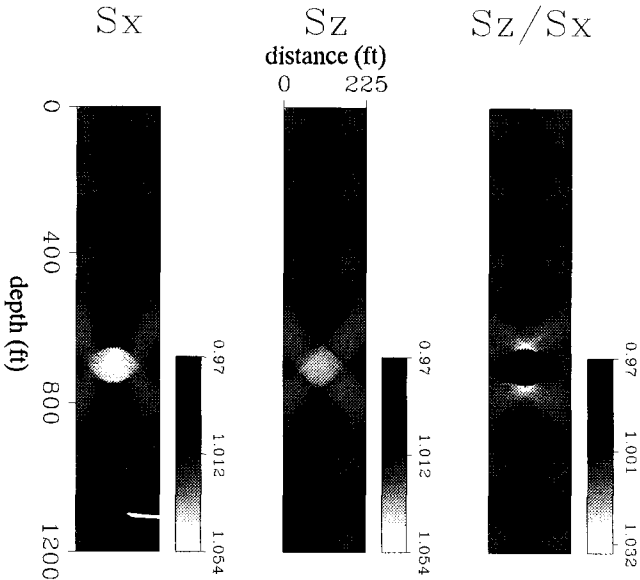


FIG. 11. Reconstructed horizontal and vertical component of the slowness. The ratio of the two components is shown at the right.

vertical component of the slowness. This is not the case in the 1D inversion, where both slowness components can be perfectly recovered even though the vertical component of the slowness is not properly sampled. The extra information introduced in that problem by assuming that the model is layered compensates for the limited view of the measurements. In the 2D inversion, where the unknown is less constrained, the better sampling of the horizontal component translates into its better recovery when compared with the vertical component and as a result, some artificial anisotropy is introduced by the reconstruction. In this noise-free example such an anisotropy is not greater than 3% as shown in Fig. 11 by the ratio S_z/S_x . Performing more CG iterations does not help to reduce this artificial anisotropy to zero, as in the 1D inversion (Figs 8 and 9). In the present case the images did not change after 120 CG iterations. This example shows that when the velocity contrasts are small, the amount of anisotropy introduced by the inversion can be of the same order as the expected heterogeneities. Similar problems may occur also when trying to estimate small variations in velocity anisotropy.

The artifacts in both slowness components are similar to the well-known truncation artifacts in isotropic inversion although they differ from one component to the other. The estimated S_x is smeared along the horizontal direction whereas S_z is not. This is because the estimation of S_z is not affected by rays that travel horizontally. The different character of the artifacts for each slowness component can limit our ability to recover variations in 'true' anisotropy at the same scale of variations in velocity when data from only one geometry is used. This will be clearly observed later in the application to field data.

FIELD DATA EXAMPLE

Anisotropic tomography was performed using a field data set. This data set was acquired jointly by Amoco Production Company and Stanford University at an on-shore Gulf Coast site in Southeast Texas. The overall survey geometry is illustrated in Fig. 12, and it is similar to the one used in the synthetic example of 2D inversion. The source (a piezo-electric bender bar) produced a sweep signal with frequencies between 400 Hz and 1600 Hz. The data were recorded with a sample interval of 0.1 ms. More details about the site and geometry are given by Harris *et al.* (1990).

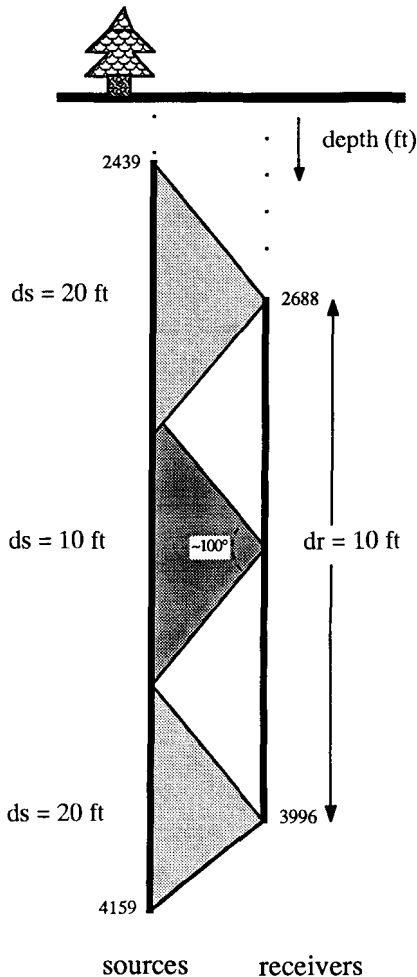


FIG. 12. Overall survey geometry illustrating the shooting pattern. Receivers are spaced at $dr = 10$ ft between 2688 and 3996 ft. Sources are spaced at $ds = 10$ ft intervals in primary target zone and $ds = 20$ ft. above and below the target zone. The average separation between wells is 225 ft.

Nearly 5000 P-wave first arrival times were picked from the correlated data. In general, we found that the traveltimes corresponding to the near horizontal rays (near offsets) were more difficult to pick than those at far offsets.

Because the shots are within $\pm 50^\circ$ with respect to the horizontal at each receiver location, we expect most of the data to be modelled appropriately by using elliptical anisotropy (Fig. 1).

To measure the goodness-of-fit between measured and calculated traveltimes, we use the root-mean-square value mismatch,

$$\text{error} = \sqrt{\frac{1}{M} \sum_{i=1}^M (t_{ci} - t_{ri})^2}, \quad (29)$$

where t_{ri} and t_{ci} are the measured and calculated traveltimes respectively and M is the total number of traveltimes.

Our inversion estimates slownesses (S_*) but we show velocities ($V_* = 1/S_*$) in the examples that follow.

Well deviation

In this particular geometry, the wells are not confined to a single plane. Instead, they deviate gradually from the vertical plane that contains both wells at the near surface. We have taken this effect into account by following this two-step procedure:

1. Find the true 3D distances between sources and receivers.
2. Assume that one well is vertical (for example, the source well) and locate the receivers at the corresponding true relative distances and true depths in the other well. This is equivalent to locating the origin of the coordinates so as to measure the distances always at the source well.

When correcting for the well deviation in this way, true source–receiver separations are used in the inversion. The relative position of the two wells after considering the deviation is shown in Fig. 13. To use the true relative distances, it is necessary to move the receiver positions horizontally in the deviated well. This is the reason why the receiver positions in Fig. 13 appear horizontally smeared. The selection of the vertical well used as a reference to measure the relative deviations is irrelevant if we assume that the model is 1D. In 2D, different distortions may occur depending on which well is chosen as a reference.

1D inversion

The simplest inversion that we can carry out is when the model is homogeneous isotropic. What we obtain is the mean velocity (equation (24)), $V_{\text{ISO}} = 8452$ ft/s. The next step is to assume that the model is still homogeneous but elliptically aniso-

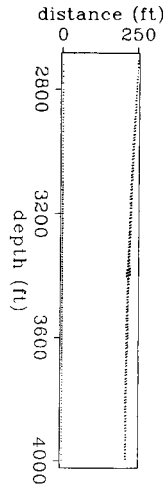


FIG. 13. Positions of the source and receiver wells after considering their relative deviations. Each dot represents a source or a receiver position (left and right respectively). Note that the density of sources is greater at the middle of the surveyed area than in the extremes.

tropic. Using (25), we find that $V_x = 8586$ ft/s and $V_{z\text{NMO}} = 8079$ ft/s. Notice that for this particular recording geometry (Fig. 12), V_{ISO} is closer to V_x than to $V_{z\text{NMO}}$, which means that the 'averaging' of the horizontal and vertical directions that the isotropic inversion implicitly carries out is not a simple arithmetic average. When the model is also heterogeneous, the same conclusion may be drawn as we show later.

Equation (29) will be used as a measure of goodness of fit of the real data when using a certain model. For the homogeneous isotropic model $error = 1.27$ ms. When the model is homogeneous anisotropic, $error = 1.17$ ms.

The result of the isotropic inversion assuming a layered medium is shown in Fig. 14. Only traveltimes corresponding to rays below 2705 ft and above 4000 ft were used. This depth interval was discretized into 60 horizontal layers of equal thickness (21.583 ft). Straight rays were used to compute synthetic traveltimes since according to Harris *et al.* (1990), small velocity variations are expected in this site. The isotropic 2D straight-ray tomogram shown in a later section is very similar to the isotropic 2D curved-ray tomogram obtained by Harris *et al.* (1990). Conjugate gradient iterations (40) were performed until no appreciable changes were seen either in the model or in the error (29). This corresponds to reaching the flat part of the hills in Fig. 8. For the model shown in Fig. 14, $error = 0.88$ ms.

We now assume the model to be anisotropic. The result of the inversion is shown in Fig. 15. For traveltimes computed with this model, $error = 0.80$ ms. The thick curve represents the horizontal velocity and the thin curve represents the vertical velocity. The first thing we notice is that as expected, V_x is generally larger than $V_{z\text{NMO}}$. Figure 16 compares V_x and $V_{z\text{NMO}}$ with V_{ISO} . In general, V_{ISO} is closer to V_x than it is to $V_{z\text{NMO}}$, which is consistent with the previous results of the inversion assuming a homogeneous medium. This means that for the type of recording

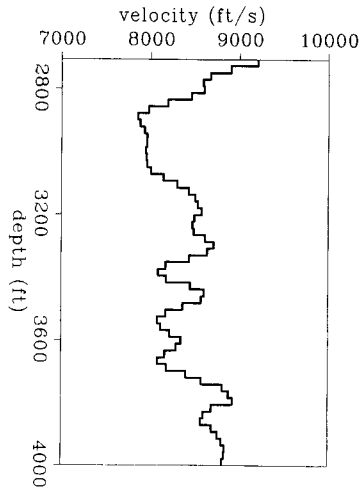


FIG. 14. Result of the isotropic layered inversion. The thickness of each layer is 21.583 ft.

geometry used (ray angles between 0 and $\pm 50^\circ$) the isotropic inversion is affected primarily by the horizontal component of the velocity. Since there are fewer rays at large angles, the isotropic inversion is less constrained by them. However, rays at large angles contain independent information that might be important in improving horizontal resolution in 2D models.

Sonic logs were available in this site at both wells (Fig. 17). They sample the vertical velocity close to the well at frequencies (~ 10 kHz) much larger than the typical frequency of the cross-well data (~ 1 kHz). To compare the information

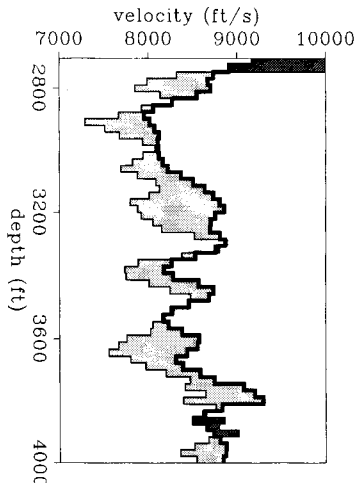


FIG. 15. Result of the anisotropic layered inversion. The thickness of each layer is 21.583 ft. The differences between V_x (thick line) and V_{zNMO} (thin line) are represented by two colours: light gray, when $V_x > V_{zNMO}$ and dark gray when $V_x < V_{zNMO}$.

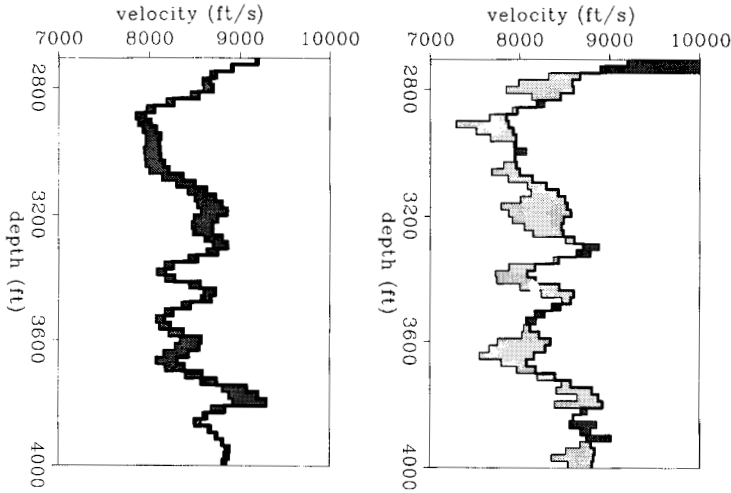


FIG. 16. Comparison between isotropic and anisotropic layered inversion. Left: V_{ISO} (thin line) and V_x (thick line). Right: V_{ISO} (thick line) and $V_{z\text{NMO}}$ (thin line). The differences between the isotropic and anisotropic inversion are represented by two colours: light gray when $V_{\text{ISO}} > V_x$ or $V_{z\text{NMO}}$, and dark gray when $V_{\text{ISO}} < V_x$ or $V_{z\text{NMO}}$.

obtained from these two types of measurements (1D tomogram and velocity logs), we performed averaging on the logs. Firstly, we averaged each slowness log in blocks of equal thickness and equal to the layer thickness in the 1D tomographic inversion. Secondly, the two averaged slowness logs were averaged again into a single one. The purpose of the last averaging was to produce a single curve to

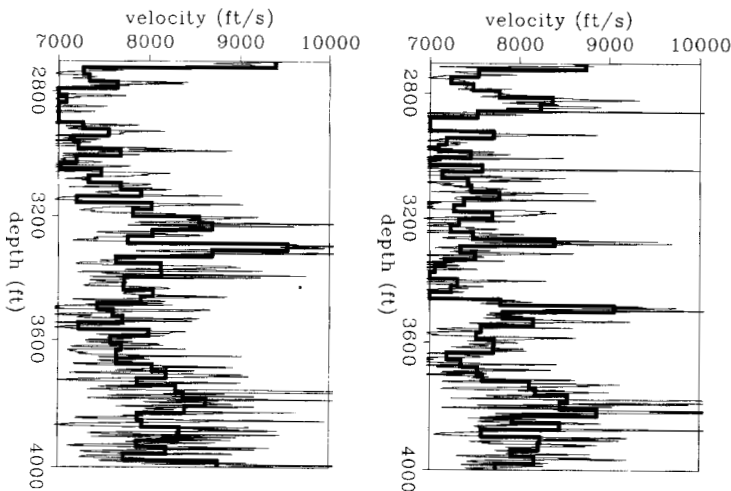


FIG. 17. Sonic logs at the source and receiver well respectively. The thin line represents the original log. The thick line represents the corresponding log averaged in 60 layers of equal thickness (21.583 ft).

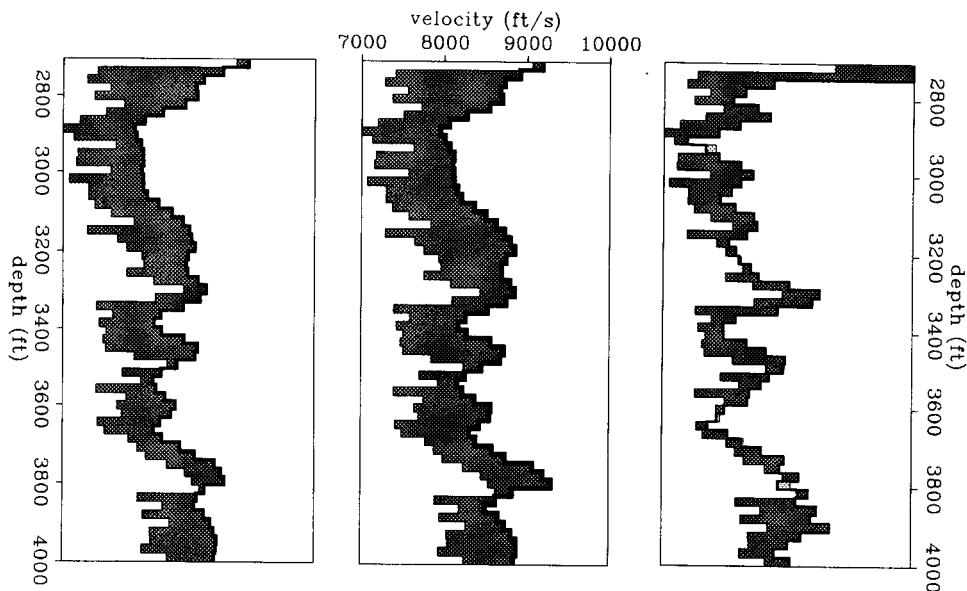


FIG. 18. Average velocity log (V_x) compared with V_{ISO} (left), V_x (centre) and V_{zNMO} (right). V_{zNMO} is closer and better correlated with the velocity log.

compare with the V_{zNMO} estimated by our algorithm. Figure 18 compares the average velocity log with V_{ISO} , V_x and V_{zNMO} . Note that V_{zNMO} is not only much closer to the average velocity log (as expected) but also better correlated with it, when compared with V_{ISO} and V_x . Figure 18 shows that the assumption of an elliptical model for the velocities is an improvement over the assumption of a circular one.

The comparison between the average velocity log and V_{zNMO} has to be interpreted carefully because each curve averages the medium velocities in a different way (in the place where the medium changes laterally). On one hand, the average log assumes that at each depth the medium has only two velocities that contribute with equal weight in the estimate (mean). On the other hand, the way the inversion averages the lateral changes in the medium properties when computing V_{zNMO} is not clear at this point. It is also not clear how the potential errors caused by inverting for 1D variations in a 2D medium propagate into the solution. The 2D nature of the true medium will be evident later when performing 2D inversion.

It can be seen in Fig. 18 that V_{zNMO} is systematically larger than the log velocity (V_z). This is exactly the opposite to what was expected from Fig. 1. We explain below different sources of biases in the inversion that may explain this unexpected result.

The ratio V_x/V_{zNMO} correlates roughly with the lithology, as shown in Fig. 19. In this figure, the thick line corresponds to the ratio V_x/V_{zNMO} and the thin line corresponds to the average spontaneous potential (SP) log. The average SP log was obtained by blocking each log separately, taking the average of the results and

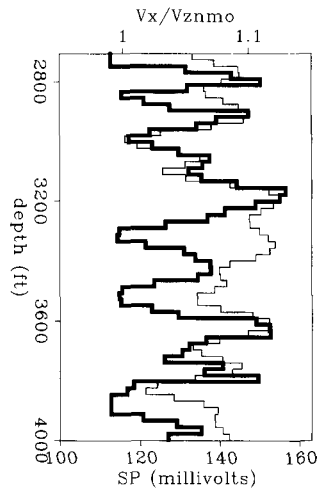


FIG. 19. Anisotropy ratio $V_x/V_{z\text{NMO}}$ (thick line) compared with the SP log (thin line).

removing a linear trend with depth in the final average. Note the good correlation between large SP values (shales) and large anisotropy ratio, and between low SP values (sands) and isotropic layers. However, remember that both curves represent a different type of averaging of the lateral changes in medium properties.

In the anisotropic inversion, we found that for this particular data set, 60 layers of 21.583 ft each was a good compromise between resolution and stability. Reducing the layer thickness by half has the effect (not shown) of increasing the resolution at the expense of large variations and instabilities in the vertical component of the velocity that is not well sampled by the recording geometry. The horizontal component of velocity is generally more stable than the vertical for smaller layer thicknesses. Obviously, increasing the layer thickness made the inversion more stable at the expense of less resolution.

2D inversion

When the relationship between the data and the unknown is linear, we should obtain the model that 'best' fits the data in only one solution of the ray-tracing problem. When the problem is non-linear one approach is to solve it as a sequence of linearized steps. We usually call these steps *external* iterations, to differentiate them from the *internal* iterations needed to solve each linear problem when using iterative techniques such as conjugate gradients. Ideally, if the problem has n unknowns, each external iteration should consist of m CG steps (m internal iterations), where $m \leq n$ is the number of different singular values. When dealing with field data, however, we might not be able to do this because of the presence of the noise. Noise can affect the solution of each linearized problem in the following ways: (a) it might be amplified into the model by the smallest singular values recovered when m iterations are performed; (b) it might affect considerably the accuracy

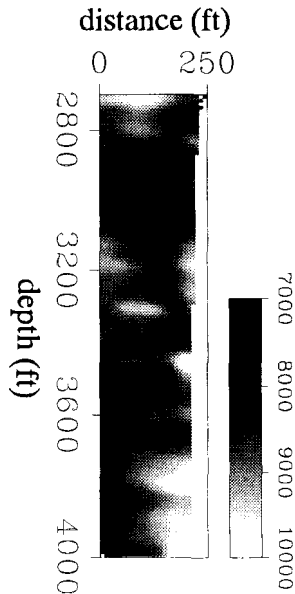


FIG. 20. Isotropic 2D inversion. The image has been divided into 131×26 square cells (10×10 ft² each).

of the search directions and consequently, the position of the minimum associated with the solution. Therefore, we have to deal carefully with noise.

Under the straight-ray assumption, only one external iteration was needed in the 1D inversion to find the model shown in Fig. 15. By selecting the layer thickness appropriately, we were able to perform the CG iterations required to reach convergence without being much affected by noise: thicker layers damped the solution whereas thinner layers introduced instabilities. In 2D, however, the situation is different. We found here that the results were more sensitive to noise in the data than 1D results. This is not surprising because now we are trying to estimate horizontal variations in $S_{z\text{NMO}}$ which, as explained before, are related to the smallest singular values of the problem (that amplify the noise).

Because of the sensitivity to noise of the 2D inversion, it is necessary to avoid 'many' CG iterations at each linearized step. After several tests combining in different ways external and internal iterations with mean-average smoothing of the slowness model, we adopted a conservative approach to minimize the error (29). The approach consisted of the following steps:

- (1) Compute traveltimes in the given model, calculate the matrix \mathbf{J} and find the residuals.
- (2) Approximate the solution of the linear problem (28) by applying a few (typically one or two) CG iterations.
- (3) Smooth the updated slowness model.
- (4) Repeat the previous steps until there is no reduction in the sum (29).

When this happens, either quit or increase the number of CG iterations by one and check if further reductions in the mismatch are obtained. When the problem is linear, the solution is not obtained in one iteration only due to the presence of the noise.

When the previous procedure was applied to estimate an isotropic model from the data, we obtained the image shown in Fig. 20 ($error = 0.76$ ms). In this case, the unknown model was discretized into 131×26 square cells (10×10 ft² each). It is interesting to notice that adding more degrees of freedom in structure (more cells) does not substantially improve the parameter $error$ obtained with 28 times less degrees of freedom in the 1D anisotropic inversion. The model shown in Fig. 20 is very similar to the one obtained by Harris *et al.* (1990), where ray bending has been taken into account.

The result of the anisotropic 2D inversion is shown in Fig. 21 ($error = 0.60$ ms). Note that V_x is remarkably similar to V_{ISO} , as in the 1D example. The main difference between these two images is that in V_x (Fig. 21) the events tend to be more horizontally smeared than in V_{ISO} (Fig. 20). This was expected from the synthetic example shown in Fig. 11.

The events in the estimated vertical component of the velocity tend to be smeared in the direction of the steepest rays and the spatial resolution in this component is poor when compared with V_{ISO} and V_x . This is because V_z is not adequately sampled by the recording geometry. In the 1D case, this lack of information

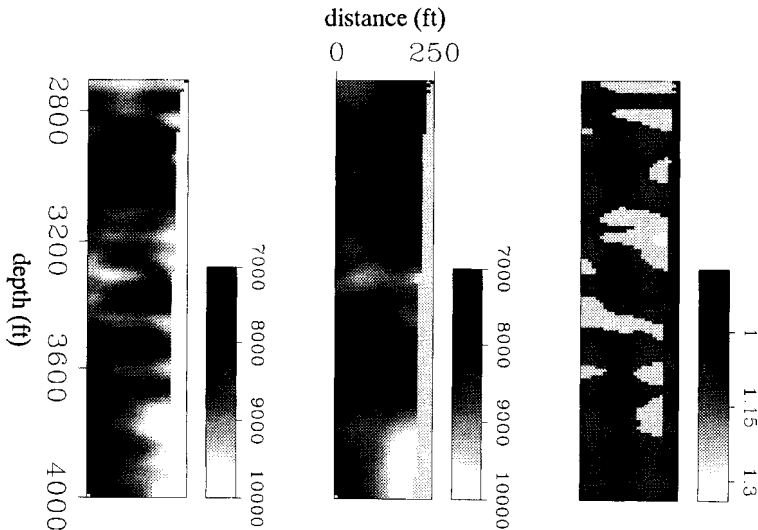


FIG. 21. Anisotropic 2D inversion. Each image has been divided into 131×26 square cells (10×10 ft² each). Left: V_x . Centre: V_{zNMO} . Right: V_x/V_{zNMO} . The spatial resolution of V_{zNMO} is poor when compared with the spatial resolution of V_x . The ratio V_x/V_{zNMO} has been separated in four areas that show percentages of anisotropy: white (ratio > 1.25), light gray ($1.06 < \text{ratio} \leq 1.25$), dark gray ($0.90 < \text{ratio} \leq 1.06$) and black (ratio ≤ 0.9). The dark gray areas can be considered isotropic.

is compensated by assuming a layered model, which allows us to perform more CG iterations without having problems with noise. In 2D this is not possible and therefore, the results can be obtained where V_x is close to convergence but $V_{z\text{NMO}}$ is far from that point. This in turn may introduce artificial anisotropy.

Because V_x and $V_{z\text{NMO}}$ cannot be estimated at the same resolution (at least using only this type of recording geometry), it is not possible to estimate spatial variations in velocity anisotropy (the ratio $V_x/V_{z\text{NMO}}$ for example) at the same scale of the variations in velocity. Even so, an image that shows variations in velocity anisotropy can be useful if it accounts only for the large-scale variations that are well resolved by the inversion. Such an image is shown in Fig. 21. This image is divided into four areas: highly anisotropic, moderately anisotropic, isotropic and anisotropic with $V_{z\text{NMO}} > V_x$. We can see that most of the model is isotropic whereas the anisotropic areas are associated with high-velocity zones, possibly shales.

Figure 22 summarizes how the mismatch estimated by (29) (*error*) changes for the different parametrization used. The error decreases roughly 40% from the homogeneous to the 1D inversion and about 50% from the homogeneous to the 2D inversion. This means that for this data set, by trying to estimate lateral variations in the medium (small singular values) a 10% reduction in the mismatch is gained with respect to estimating *only* vertical variations in the model (largest singular values). Note also that mismatch is not substantially reduced when comparing the 1D anisotropic inversion (letter D in the plot) with the 2D isotropic (letter E), with 28 more degrees of freedom. Equivalently, this suggests that anisotropy in the data can be reconciled with either isotropic heterogeneity or anisotropic less heterogeneous media.

Biases in the inversion

The main problem considered in the previous sections was how the limited view of the measurements affects our ability to estimate velocities in different directions. By assuming elliptical anisotropy it was necessary to estimate only two velocities:

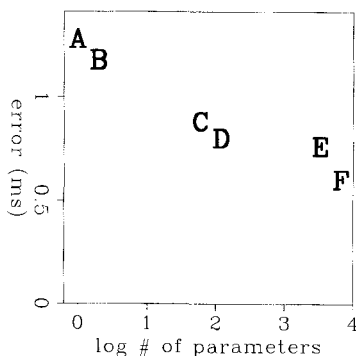


FIG. 22. Errors for the different parametrizations. (A) Homogeneous isotropic; (B) homogeneous anisotropic; (C) 1D isotropic; (D) 1D anisotropic; (E) 2D isotropic; (F) 2D anisotropic.

horizontal and vertical. Of course, this is too simple to describe the real complexities of the velocities in many cases but it is the first step beyond fitting the data with circles (isotropic tomography). Unless we considerably constrain the inversion (layered models) or we have measurements from a wide range of angles, it is difficult to estimate *accurately* and *simultaneously* S_x and $S_{z\text{NMO}}$. Unfortunately, even with constraints and wide-angle measurements, many other factors may affect the results.

Among these factors we have:

- Picking errors. These errors may systematically increase or decrease the velocities, depending on which part of the first arriving wavelet has been picked. Picking before the correct value speeds up velocities whereas picking later slows them down. This may explain why, in Fig. 15, $V_{z\text{NMO}}$ is systematically 1 or 2% faster than the sonic log.
- Well deviation. The wells deviate in 3D but we decided to work in 2D. If the real 3D variations in the medium are moderate, this is a good approximation, but it may not be otherwise. When first testing our algorithm with real data the well deviation was not considered. We simply substituted each well by a vertical one located at its average surface location. The results (not shown) were higher velocities (than those shown in Fig. 12) where the wells were actually closer and lower velocities where the wells were actually farther apart. Considering the well deviation affected S_x more than $S_{z\text{NMO}}$.
- Head waves versus body waves. Although this may be considered a picking error, it primarily affects traveltimes at vertical near offsets (small ray angles) in low-velocity layers. These errors mainly affect the estimation of S_x because $S_{z\text{NMO}}$ does not use information from rays that travel at small angles. In principle, when head waves are inverted like body waves, the estimated horizontal velocity turns out to be faster than the real one.
- Ray bending. When not considered, it can introduce errors in the estimation of velocity anisotropy in places where the velocity contrasts are large.

All the previous factors, when not considered appropriately, may produce artificially anisotropic results. For this reason and the ill-conditioning of the problem studied later, the estimation of small-scale 2D variations in velocity anisotropy is a difficult task.

CONCLUSIONS

We have presented the basic theory and examples of an algorithm that performs anisotropic traveltome tomography. The algorithm generalizes the well-known techniques of tomographic traveltome inversion by using models discretized into a set of homogeneous, elliptically anisotropic cells, where each cell is characterized by two slownesses, one vertical and the other horizontal. Both components of the slowness can be estimated simultaneously provided that the range of ray angles is great enough. Otherwise the problem becomes ill-conditioned. As expected for cross-well geometries, it is more difficult to estimate the vertical component of the slowness. In

particular in 2D, the estimated vertical component of the slowness may have such a poor resolution that it is difficult to estimate the spatial variations of velocity anisotropy at the same scale of velocity heterogeneities.

Due to the limited view of the measurements, when iterative techniques such as conjugate gradients are used to estimate velocity anisotropy, early termination of the iterations may produce artificial anisotropy. This is more severe in 2D than in 1D estimation of velocity anisotropy.

If traveltimes for P-, SV- and SH-waves from cross-well and VSP geometries are available, anisotropic tomography as we propose it can be used within the framework of the double elliptical approximation to estimate 1D and 2D variations of the elastic constants.

ACKNOWLEDGEMENTS

We thank Amoco Production Company, the Gas Research Institute and the Seismic Tomography Project at Stanford University for acquiring and providing the data. We also thank Joe Dellinger for preparing the figures related to the double elliptic approximation. The first author thanks INTEVEP, S.A. for financial support. The reviewers' comments and suggestions are also gratefully acknowledged.

APPENDIX

DERIVATION OF THE DOUBLE ELLIPTIC APPROXIMATION

First we define some new symbols:

$$\begin{aligned} c &= \cos(\theta), \\ s &= \sin(\theta), \\ \theta &= \text{group angle from the vertical,} \\ C &= \cos(\phi), \\ S &= \sin(\phi), \\ \phi &= \text{phase angle from the vertical.} \end{aligned}$$

It has been shown (Levin 1978; Byun 1982) that a phase-velocity expression of elliptical shape,

$$W(\theta) = W_x s^2 + W_z c^2, \quad (\text{A1})$$

leads to a ray-velocity expression of elliptical shape,

$$M(\phi) = M_x S^2 + M_z C^2, \quad (\text{A2})$$

where

$$M_* = \frac{1}{W_*}. \quad (\text{A3})$$

The previous expression for the dispersion relation can be written as

$$\begin{aligned}
 W(\theta) &= \frac{(W_x s^2 + W_z c^2)^3}{(W_x s^2 + W_z c^2)^2} \\
 &= \frac{W_x^3 s^6 + W_x^2(3W_z)s^4 c^2 + W_x^2(3W_x)c^4 s^2 + W_z^3 c^6}{(W_x s^2 + W_z c^2)^2}
 \end{aligned} \tag{A4}$$

If the quantities $3W_z$ and $3W_x$ are approximated as follows

$$\begin{aligned}
 3W_x &\approx 2W_x + W_{x\text{NMO}}, \\
 3W_z &\approx 2W_z + W_{z\text{NMO}},
 \end{aligned} \tag{A5}$$

it results in the double elliptical approximation:

$$W(\theta) = \frac{W_x^3 s^6 + W_x^2(2W_z + W_{z\text{NMO}})s^4 c^2 + W_z^2(2W_x + W_{x\text{NMO}})s^2 c^4 + W_z^3 c^6}{(W_x s^2 + W_z c^2)^2} \tag{A6}$$

To understand the meaning of the NMO parameters introduced in (A5), we expand (A6) around $\theta = 0$, keeping only terms up to c^2 . After some algebra we obtain

$$W(\theta) = W_z c^2 + W_{x\text{NMO}} s^2.$$

After expanding around $\theta = \pi/2$, we get (keeping only terms up to s^2)

$$W(\theta) = W_{z\text{NMO}} c^2 + W_x s^2.$$

We see that the NMO parameters are obtained by fitting the slowness surface with ellipses around horizontal and vertical axes. If the true wave surface is elliptical, the NMO parameters are equal to the real ones but otherwise they simply describe, along with the true slownesses, the best-fitting ellipses around the axis of symmetry and perpendicular to it.

Note that in (A6) the phase velocity is a combination of four parameters, as well as the exact expression for phase velocity (for P- and SV-waves) that is a combination of four elastic constants. The reader might wonder about the usefulness of an approximation that has the same number of parameters as the exact expression. The difference is that in the exact expression the *estimation* of the parameters (elastic constants) is difficult whereas in the approximate one it is simple because of their simple relationship with ray slownesses along the axes (A3).

Equation (A6) comes from approximating (A4) by introducing the NMO phase velocities W_* . Equation (A4) comes from (A1) after evaluating the following expression at $n = 2$:

$$W(\theta) = \frac{(W_x s^2 + W_z c^2)^{n+1}}{(W_x s^2 + W_z c^2)^n}. \tag{A7}$$

Different values of n will produce approximations more or less accurate than (A6). For example, when $n = 1$ the result is a three-parameter approximation for the phase velocities that is less accurate than the double elliptical approximation. This issue is explained in detail by Dellinger *et al.* (1993).

By following the same steps as before but starting from (A2), we obtain the approximation for the ray slowness squared:

$$M(\phi) = \frac{M_x^3 C^6 + M_x^2(2M_z + M_{z\text{NMO}})C^4 S^2 + M_z^2(2M_x + M_{x\text{NMO}})C^2 S^4 + M_z^3 S^6}{(M_x C^2 + M_z S^2)^2} \quad (\text{A8})$$

REFERENCES

- AULD, B.A. 1990. *Acoustic Fields and Waves in Solids: Vol. 1*. Robert E. Krieger Publishing Co.
- BANIK, N.C. 1984. Velocity anisotropy of shales and depth estimation in the North Sea basin. *Geophysics* **49**, 1411–1419.
- BREGMAN, N.D., BAILEY, R.C. and CHAPMAN, C.H. 1989. Ghosts in tomography: the effect of poor angular coverage in 2-D seismic travelt ime inversion. *Canadian Journal of Exploration Geophysics* **25**, 7–27.
- Byun, B.S. 1982. Seismic parameters for media with elliptical velocity dependencies. *Geophysics* **47**, 1621–1626.
- BYUN, B.S. and CORRIGAN, D. 1990. Seismic travelt ime inversion for transverse isotropy. *Geophysics* **55**, 192–200.
- CHAPMAN, C.H. and PRATT, R.G. 1992. Travelt ime tomography in anisotropic media: theory. *Geophysical Journal International* **109**, 1–19.
- DELLINGER, J. 1989. Anisotropic travelt ime inversion with error bars: theory. *Stanford Exploration Project* **60**, 253–260.
- DELLINGER, J., MUIR, F. and KARRENBACH, M. 1992. Anelliptic approximations for TI media. *Journal of Seismic Exploration*, in press.
- GILL, P.E., MURRAY, W. and WRIGHT, M.H. 1991. *Numerical Linear Algebra and Optimization: Vol. 1*. Addison-Wesley Pub. Co.
- HARRIS, J.M., TAN, H., LINES, L., PEARSON, C., TREITEL, S., MAVKO, G., MOOS, D. and NOLEN-HOEKSEMA, R.J. 1990. Cross-well tomographic imaging of geological structures in Gulf Coast sediments. *60th SEG meeting, San Francisco, Expanded Abstracts*, 37–40.
- LEVIN, F.K. 1978. The reflection, refraction, and diffraction of waves in media with elliptical velocity dependence. *Geophysics* **43**, 528–537.
- MCMECHAN, G.A. 1983. Seismic tomography in boreholes. *Geophysical Journal of the Royal Astronomical Society* **74**, 601–612.
- MICHELENA, R.J., 1993. Singular value decomposition for cross-well tomography. *Geophysics*, in press.
- MUIR, F. 1990. A modified anisotropic system. *Stanford Exploration Project* **67**, 41–42.
- MUIR, F. 1991. Various equations for TI media. *Stanford Exploration Project* **70**, 367–372.
- NOLET, G. 1987. Seismic wave propagation and seismic tomography. In: *Seismic Tomography*. G. Nolet (ed.), 1–23. D. Reidel Pub. Co.
- PRATT, R.G. and CHAPMAN, C.H. 1992. Travelt ime tomography in anisotropic media: application. *Geophysical Journal International* **109**, 20–37.
- STEWART, R.R. 1988. An algebraic reconstruction technique for weakly anisotropic velocity. *Geophysics* **53**, 1613–1615.
- THOMSEN, L. 1986. Weak elastic anisotropy. *Geophysics* **51**, 1954–1966.
- WHITE, J.E., MARTINEAU-NICOLETIS, L. and MONASH, C. 1983. Measured anisotropy in Pierre shale. *Geophysical Prospecting* **31**, 707–725.
- WINTERSTEIN, D.F. 1986. Anisotropy effects in P-wave and SH-wave stacking velocities contain information on lithology. *Geophysics* **51**, 661–672.
- WINTERSTEIN, D.F. and PAULSSON, B.N. 1990. Velocity anisotropy in shale determined from crosshole seismic and vertical seismic profile data. *Geophysics* **55**, 470–479.